PCCP

ROYAL SOCIETY OF CHEMISTRY

ARTICLE TYPE

Cite this: DOI: 10.1039/xxxxxxxxxx

Shear heating, flow, and friction of confined molecular fluids at high pressure†

James P. Ewen,*‡[a] Hongyu Gao,‡[a,b] Martin H. Müser[b] and Daniele Dini[a]

Received Date
Accepted Date

DOI: 10.1039/xxxxxxxxxx

www.rsc.org/journalname

Understanding the molecular-scale behavior of fluids confined and sheared between solid surfaces is important for many applications, particularly tribology where this often governs the macroscopic frictional response. In this study, nonequilibrium molecular dynamics simulations are performed to investigate the effects of fluid and surface properties on the spatially resolved temperature and flow profiles, as well as friction. The severe pressure and shear rate conditions studied are representative of the elastohydrodynamic lubrication regime. In agreement with tribology experiments, flexible lubricant molecules give low friction, which increases linearly with logarithmic shear rate, while bulky traction fluids show higher friction, but a weaker shear rate dependence. Compared to lubricants, traction fluids show more significant shear heating and stronger shear localization. Models developed for macroscopic systems can be used to describe both the spatially resolved temperature profile shape and the mean film temperature rise. The thermal conductivity of the fluids increases with pressure and is significantly higher for lubricants compared to traction fluids, in agreement with experimental results. In a subset of simulations, the efficiency of the thermostat in one of the surfaces is reduced to represent surfaces with lower thermal conductivity. For these unsymmetrical systems, the flow and the temperature profiles become strongly asymmetric and some thermal slip can occur at the solid-fluid interface, despite the absence of velocity slip. The larger temperature rises and steeper velocity gradients in these cases lead to large reductions in friction, particularly at high pressure and shear rate.

1 Introduction

From the design of nanofluidic devices[1] to improving lubricant performance,[2] understanding the molecular-scale behavior of fluids confined and sheared between solid surfaces is of significant importance.[3] The latter is of particular interest since it has the potential to substantially reduce friction losses in engineering components and thus minimize CO_2 emissions.[4] Many lubricated engineering components include elements with non-conforming surfaces that roll and slide together, for example; rolling bearings, gears, constant velocity joints and cam/follower systems. In these components, a significant proportion of the friction loss is in the elastohydrodynamic lubrication (EHL) regime, where very thin (nm) fluid films are sheared at very high shear rate, $\dot{\gamma}$ (10^5-10^8 s^{-1}) and pressure, P (GPa).[5] Such extreme conditions are difficult to investigate with *in situ* experiments and thus prediction of EHL friction remains a considerable challenge.[5]

Under EHL conditions, a large amount of energy is dissipated within the fluid film and this can lead to large rises in local temperature, T.[5,6] The Archard equation[7] is commonly used to predict the T rise under EHL conditions, although the choice of some parameters is still debated.[5] The T rise at the solid surfaces and within the fluid film has been studied experimentally using *in situ* infrared (IR) microscopy under EHL conditions.[8–10] Recently, IR microscopy has shown that the shape of the spatially resolved T profile in the fluid film can become asymmetrical when surfaces with different thermal properties are employed.[10] This is important for contacts in which one of the surfaces is coated with a thermally insulating material such as diamond-like-carbon (DLC)[11,12] and ceramics,[13] which have both been shown to significantly reduce friction.

It has also been suggested that the severe EHL conditions could lead to non-linear fluid flow which deviates from the commonly assumed Couette case.[14] Indeed, shear localization, where different regions of fluid flow faster than others, has been reported for a range of viscous fluids at high P.[5] For example, shear localization has been experimentally observed in relatively thick ($\approx 100\ \mu$m)

[a] *Department of Mechanical Engineering, Imperial College London, London SW7 2AZ, UK. Email: j.ewen@imperial.ac.uk*
[b] *Department of Materials Science and Engineering, Universität des Saarlandes, 66123 Saarbrücken, Germany*

† Electronic Supplementary Information (ESI) available: atomic mass density profiles, average fluid density, additional temperature profiles, and additional flow profiles.. See DOI: 10.1039/cXCP00000x/

‡ These authors contributed equally to this work.

viscous polymer films at high P.[15–17] More recently, shear localization has been observed in thinner (≈ 1 μm) viscous polymer films under conditions more representative of EHL using *in situ* photoluminescence techniques.[18–20] However, such behavior has not yet been demonstrated experimentally using both representative EHL conditions and fluids similar to commercial lubricants.[5]

Lubricants are designed to give low EHL friction to minimize energy losses while traction fluids should give consistently high friction for use in continuously variable transmissions.[21] For the rational design of lubricants, traction fluids, and surfaces to control EHL friction, a detailed understanding of their molecular-scale behavior is required. This is difficult to obtain from experiments alone, and confined nonequilibrium molecular dynamics (NEMD) simulations[22] have provided insights into this behavior under EHL conditions.[23] For example, comprehensive confined NEMD simulations have studied the shear heating, flow, and friction behavior of atomic Lennard-Jones (LJ) fluids at high P and $\dot{\gamma}$.[24–26] As observed experimentally,[18–20] transitions between Couette flow and different forms of shear localization were reported as P was increased.[24–26] Shear localization has also been observed in NEMD simulations of many other fluids such as model glasses[27] and entangled polymer melts.[28] Bulk NEMD simulations of lubricant molecules have shed light on their nonlinear rheological behavior under EHL conditions;[29–31] however, shear localization cannot be captured in such simulations since a linear velocity profile is imposed on the system.[23,28] Recently, the shear localization and friction of realistic lubricant and traction fluid molecules have also been investigated with confined NEMD simulations under EHL conditions.[32–34] These simulations have demonstrated links between the flow and friction behavior, which can both deviate significantly from that commonly assumed in macroscale models for EHL.

Several uncertainties still persist regarding the effects of molecular structure and surface properties on shear heating, flow, and friction under EHL conditions.[5] In this study, this behavior will be investigated simultaneously using NEMD simulations of lubricants and traction fluids confined between Fe surfaces at extreme P and $\dot{\gamma}$ conditions. In our previous study,[32] we focused on isothermal conditions in both the tribology experiments and the NEMD simulations. Conversely, in this current NEMD study, particular attention will be paid towards non-isothermal conditions where significant shear heating occurs within the fluid film.[35] The resultant spatially resolved T profiles will be used to investigate the thermal conductivity of the molecular fluids, λ_f, as they have been for LJ fluids.[24,25] This will allow the applicability of macroscale models for EHL film T rise to be tested at the molecular-scale. Results are presented for symmetrical systems, in which both surfaces have high thermostat efficiency, and unsymmetrical systems, where one surface has lower thermostat efficiency. The latter case is used to investigate the effect of contacts in which one of the surfaces is coated with an insulating material with low thermal conductivity. The molecular-scale insights provided improve fundamental understanding of shear heating, flow and friction under EHL conditions.

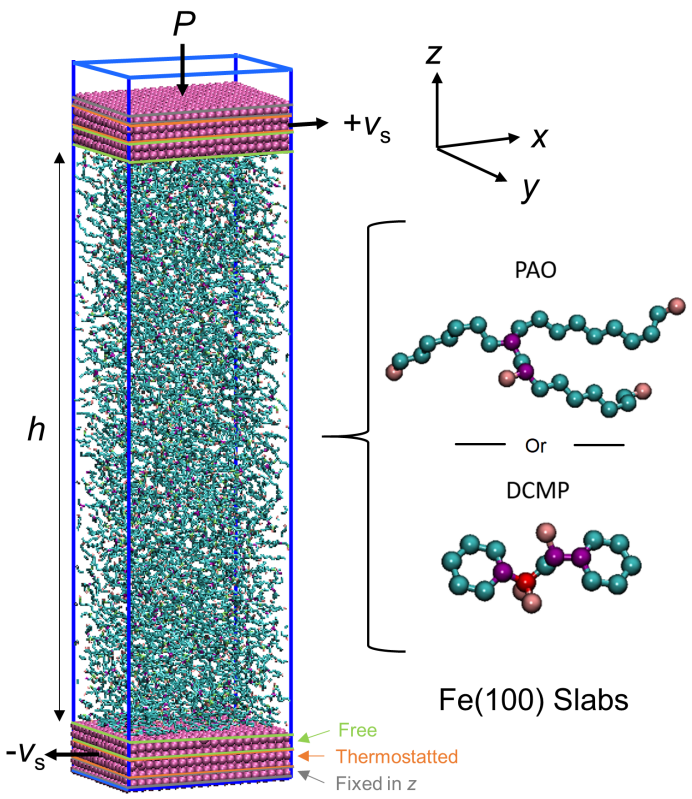

Fig. 1 Representative NEMD system with molecular structure of the studied fluids shown. Visualized with VMD.[38]

2 Methodology

2.1 Simulation Setup

MD simulations were performed using the open source Large-scale Atomic/Molecular Massively Parallel Simulator (LAMMPS) software.[36] The MD equations of motion were integrated using the velocity-Verlet algorithm with a time step of 2 fs.[37] All of the systems were constructed using the Materials and Processes Simulations (MAPS) platform from Scienomics SARL. They consisted of two parallel, atomically-smooth α-Fe(100) slabs (as a model for steel), separated by a fluid layer with a film thickness, $h \approx 22$ nm at 0.1 MPa, as shown in Fig. 1. The x, y, z dimensions of the slabs were 5.71, 4.28, 1.43 nm respectively. Periodic boundary conditions were applied in the xy-plane. The fluid was confined in the z-direction by the slabs.

Two fluid molecules were studied; hydrogenated 1-decene trimer, the major component of 4 cSt at 100 °C poly-alpha-olefin (PAO)4 lubricant,[30] and 2,4-dicyclohexyl-2-methylpentane (DCMP), a traction fluid marketed as Santotrac 2000 (formerly Santotrac 40).[21,32] Both are well-characterized fluids and their molecular structures are shown in Fig. 1. The fluid molecules were randomly inserted between the slabs using the 'Amorphous Builder' module in MAPS. The total number of PAO and DCMP molecules are 820 and 889, respectively, such that h was similar for both fluids at ambient P.

For the fluid molecules, the Transferable Potentials for Phase Equilibria-United Atom (TraPPE-UA) force-field[37] was used to de-

scribe both the bonded and non-bonded interactions. A harmonic potential was used for bond stretching (rather than rigid bonds), with parameters taken from AMBER-UA,[39] as suggested for MD simulations on the TraPPE website.[40] Bond bending (bond angle) and the bond torsion (dihedral angle) were also described using harmonic functions.[37] A 12-6 LJ potential[41] was used for the non-bonded interactions, with a cut-off distance of 1.4 nm.[37] The Lorentz-Berthelot mixing rules[42,43] were used to determine LJ cross interactions, as prescribed in the TraPPE force-field.[37] TraPPE-UA parameters developed specifically for linear,[37] branched (for both fluids)[44] and cyclic (for DCMP)[45] alkanes were employed.[40]

In UA force-fields, the CH, CH_2, and CH_3 groups are treated as single pseudoatoms to reduce the number of interaction sites. For the alkanes studied here, all of the pseudoatoms are electronically neutral, so there is no requirement to calculate long-range electrostatic forces. Combined with the larger time step possible, these factors decrease the computational expense by more than an order of magnitude compared to all-atom (AA) force-fields,[37]. To verify the force-field for the fluids used here, it was first ensured that simulated densities were close to the experimental value at $T = 313$ K and $P = 0.1$ MPa using the bulk isothermal-isobaric (NPT) procedure described in ref.[46] The density of both fluids, ρ_f; 0.78 g cm^{-3} for PAO and 0.85 g cm^{-3} for DCMP were within 4 % of the experimental values of 0.80 g cm^{-3} for PAO[30] and 0.89 g cm^{-3} for DCMP.[6] However, UA force-fields have been shown to significantly under-predict the η of long n-alkanes.[46,47] From previous simulations of similar molecules, the viscosity of the fluids is expected to be approximately 40 % lower than experiment.[30,48] However, the pressure-viscosity coefficient (α) is expected to be accurately reproduced.[30,48] Indeed, the friction results shown in the Section 3.3. agree well with NEMD simulations using an AA force-field as well as extrapolations from tribology experiments.[32] The use of a UA force-field was thus considered to be an acceptable trade-off between accuracy and computational expense for the wide parameter study conducted here.[23,31]

In the α-Fe(100) slabs, interactions were described by the embedded-atom method (EAM) with parameters taken from ref.[49] For the interactions between the Fe atoms and the fluids, initial LJ parameters were modified from ref.[50] The Fe ε parameter (depth of the potential well) was increased to 18.9 kcal mol^{-1} to prevent boundary slip on the atomically-smooth surfaces.[32,34,50] This only affects the dynamics of molecules adjacent to the surface since the Fe σ parameter (inter-atomic distance at which interaction is zero) remains unchanged at 0.2321 nm.[50] Moreover, previous studies have shown that the flow and friction behavior remain unchanged upon increasing ε once boundary slip is prevented.[34,50]

In triblogy experiments, there is significant variation in the P and $\dot{\gamma}$ conditions within the contact[51,52] and these cannot all be captured in NEMD simulations which are limited to the nanoscale.[53] However, good agreement between tribology experiments and NEMD simulations performed under average conditions for the contact have confirmed the applicability of this approach.[32,34] Even at the highest P studied (1.0 GPa), $h \approx 20$ nm, and the spatially resolved (z) atomic mass density profiles show that no layering is evident in the center of the fluid (see ESI), suggesting a negligible increase in fluid viscosity, η, due to confinement.[54] This assumption is also supported by recent resonance shear measurement experiments of thin PAO films between smooth Fe surfaces.[55] The friction results from the NEMD simulations are thus expected to be insensitive to h.[32,34] Consequently, the NEMD simulations are representative of macroscopic tribology experiments in the EHL regime in which h is much greater than the composite surface roughness such that negligible asperity contact occurs.[21,32]

2.2 Simulation Procedure

First, the systems were energy minimized and then equilibrated at the target T (350 K), with the bottom slab fixed in z and the top slab free to move. The P was then increased by applying a constant normal force to the outer layer of atoms in the top slab while keeping the outer layer of atoms in the bottom slab fixed in z (see Fig. 1).[56] The values of P considered were between 0.5-1.0 GPa, which are representative of the EHL regime,[5] and are expected to straddle the glass transition P for DCMP at 350 K.[57] Initially, the slab separation varied in a damped harmonic manner, so sliding was not applied until h fluctuated by less than 1 % around a steady state mean value.[32,56] These compression simulations were generally approximately 1 ns in duration.

After compressive oscillation became negligible, a shear velocity gradient was imposed on the fluid by applying a constant sliding velocity, $v_x = \pm v_s/2$, to the outermost layer of atoms in each slab (grey boxes in Fig. 1) in the x direction. Applying the velocity gradient in this manner, rather than directly to the fluid atoms,[29–31] is necessary to capture any shear localization behavior.[28] Sliding simulations were conducted until the T and flow profiles, as well as the mean shear stress, $\bar{\tau}$, reached a steady state. The necessary simulation time was between 10-100 ns, with those assigned a lower v_s requiring longer to reach a nonequilibrium steady state.[32] The values of v_s applied were between 1-100 m s^{-1} and $h =$ 17-20 nm under compression and steady state sliding (depending on the fluid and conditions). The applied shear rate, $\dot{\gamma} = v_s/h$ so here $\dot{\gamma} \approx 10^7$-$10^{10}$ s^{-1}. Although lower values of $\dot{\gamma}$ are desirable to overlap with those used in tribology experiments and real components,[58] they are not computationally feasible for extensive parameter studies.[23,32]

The T was controlled using a Langevin thermostat[59] set to 350 K, which is representative of the EHL regime.[5] The thermostat acted only in the direction perpendicular to both sliding and compression (y).[32,35] The thermostat was applied only to the middle layer of slab atoms (orange boxes in Fig. 1), allowing a T gradient to develop within the fluid film due to shear heating.[60–63] Fluid film T rise is also common in tribology experiments under EHL conditions.[7–10]

In recent NEMD simulations, Langevin thermostats[59] with a range of coupling times (0.5-50 ps) were tested to reproduce the experimental thermal conductivity of α-Fe surfaces.[64] In the current simulations, the Langevin thermostat in the bottom slab was assigned a coupling time of 0.1 ps, by which a thermal conductiv-

ity similar to α-Fe surfaces (as a model for steel) was simulated.[64] In the first set of simulations, the top slab was also given a coupling time of 0.1 ps, yielding symmetrical systems with relatively efficient thermal dissipation.[32] In the second set of simulations, unsymmetrical systems in which one of the surfaces had much lower thermal conductivity compared to steel (e.g. DLC or ceramics[11–13]) were also investigated. In these unsymmetrical systems, the top slab was assigned a longer thermostat coupling time to give less efficient thermal dissipation. Quantitative relationships between the thermostat coupling time and thermal conductivity are yet to be established for surfaces other than α-Fe. Moreover, obtaining accurate experimental values of the thermal conductivity of tribological surfaces is still an area of ongoing research.[65] Therefore, in the current study, a wide range of longer coupling times (1-100 ps) were considered to capture the possible effects of different surfaces with low thermal conductivity. This range is similar to that employed in ref.[64] for thermostat parameterisation (0.5-50 ps). Results from only the most extreme case (bottom 0.1 ps, top 100 ps) are shown in the main text, while intermediate results are shown in the ESI. It is important to note that, in tribology experiments, additional considerations such as the thickness, rigidity, heat capacity, and fluid wettability of surface coatings could also influence the flow and friction behavior,[11–13] but these are not considered in these current simulations.

3 Results and Discussion

The NEMD simulations performed here provide molecular-level insights into the shear heating (Section 3.1), flow (Section 3.2) and friction (Section 3.3) behavior under EHL conditions. Results are presented for symmetrical and unsymmetrical contacts. In the latter case, the top surface has a longer thermostat coupling time to represent surfaces with lower thermal conductivity compared to α-Fe, e.g. DLC or ceramics.[11–13] Note that all results presented have reached a nonequilibrium steady state, i.e. the block averaged values no longer change over time within statistical uncertainty.

3.1 Shear Heating

For the calculation of T, the kinetic energy is block averaged such that a Gaussian distribution is obtained. For the spatially resolved profiles, the local T is spatially binned in the z-direction. The local T was derived from the x, y, and z components of the peculiar momenta kinetic energy, which are computed relative to the imposed streaming velocity.[24] The x, y and z components show no statistical difference, apart from in the layered fluid region close to the slabs (see ESI). In all of the T profiles, h is normalized between the different systems in order to aid comparison.

3.1.1 Symmetrical Systems

Fig. 2 shows a representative example of the spatially resolved NEMD T profiles for the symmetrical systems. In this symmetrical system, both slabs have a thermostat coupling time of 0.1 ps, representing efficient thermal dissipation of α-Fe (as a model for steel).[64] For all of the symmetrical systems, the T profiles are parabolic with the maximum T_f in the center of the film and the outer molecular layer of fluid at the same T as the thermostatted slabs.

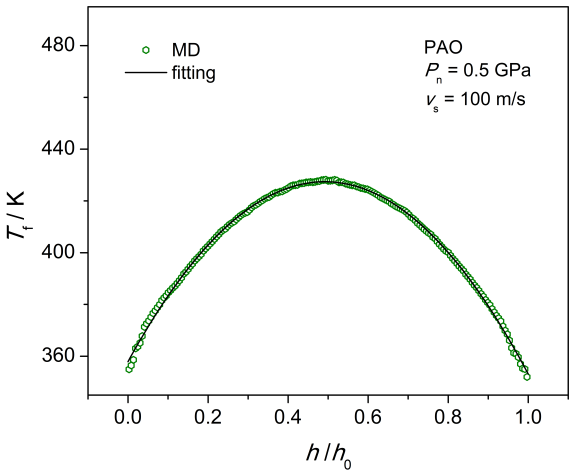

Fig. 2 Spatially resolved $T(z)$ profile for PAO at 0.5 GPa and 100 m s^{-1}. Both slabs thermostat coupling time of 0.1 ps (symmetrical system). Note that h is normalized. Solid line is quadratic fit using eqn (1).

The shape of the profiles are consistent with previous NEMD simulations of LJ fluids[24,25,60] and can be fitted quadratically using the Fourier law of heat conduction.[66] Following the analysis in refs.[24,25] the spatial T of the fluid, T_f can be rewritten as:

$$T_f = -\frac{\bar{\tau}\,\dot{\gamma}\,z^2}{2\lambda_f} + T_{s-f}, \quad 0 \le z \le z_1 \tag{1}$$

where z is the distance from the center of the film, λ_f is the thermal conductivity of the fluid, and T_{s-f} is an integration constant. The value of T_{s-f} was obtained by comparing the T of the liquid and of the solid boundary at z_1. The T of the solid slabs, T_s, is assumed to be a constant across z since the slabs are thermostatted, leading to:

$$T_{s-f} = T_s + \frac{\bar{\tau}\,\dot{\gamma}\,{z_1}^2}{2\lambda_f} \tag{2}$$

For the symmetrical systems, the T_f of the outermost regions of fluid are always within 5 K of the target T in the thermostatted slabs, so $T_{s-f} \approx T_s = 350$ K. From the NEMD simulation results, λ_f was obtained through a least-squares fit, giving the solid line in Fig. 2. In all cases, excellent agreement is obtained between the NEMD simulation data and the fitted curves, indicating that the T_f profiles can be approximated by a parabola where the curvature is determined through by the relationship: $(\bar{\tau}\dot{\gamma})/(2\lambda_f)$.[25] For clarity, the remainder of the T_f profiles presented below show only the quadratic fits of the NEMD data.

Previous thermal NEMD simulations in which a T gradient, rather than a velocity gradient, is directly imposed on the system have shown that the λ_f obtained from such simulations agrees within the numerical accuracy with that calculated using equilibrium MD using the Green-Kubo method (with no external gradient).[67] Thus, the λ_f values calculated here are expected to be consistent with other methods, despite the rather large thermal

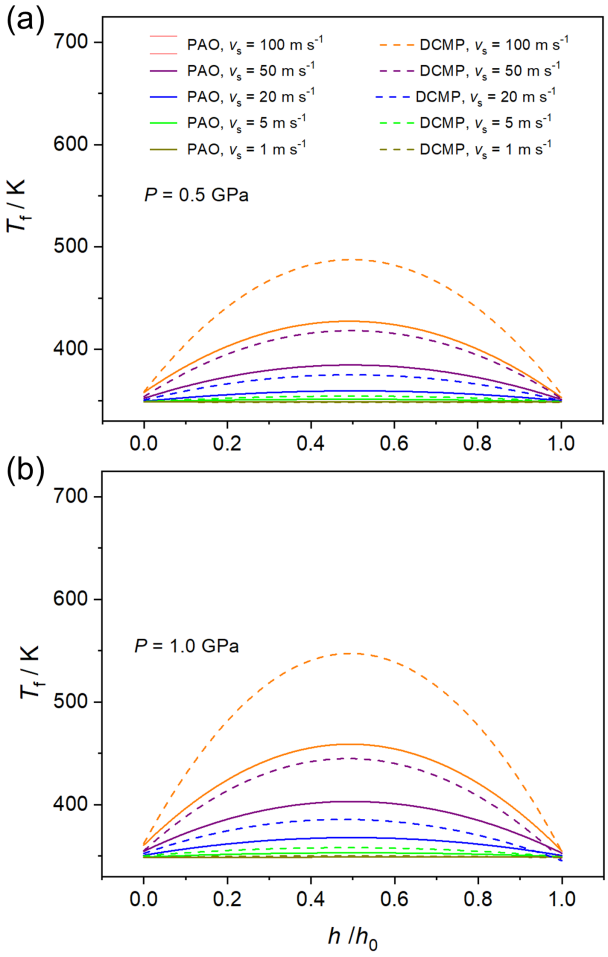

Fig. 3 Quadratic fits of the spatially resolved $T(z)$ profiles for PAO and DCMP at (a) 0.5 GPa and (b) 1.0 GPa for the different sliding velocities considered. Both slabs thermostat coupling time of 0.1 ps (symmetrical systems). Note that h is normalized.

gradients that develop at high $\dot{\gamma}$.

Fig. 3 shows quadratic fits of the T_f profiles for PAO and DCMP at (a) 0.5 GPa and (b) 1.0 GPa at the different v_s values considered for the symmetrical systems. At low v_s (1-5 m s^{-1}), the simulations can be considered isothermal since there is a negligible increase in T_f, which is within 10 K of the target value (350 K).[32,35] Generally, larger increases in T_f occur; i) at higher v_s, ii) at higher P, and iii) for DCMP compared to PAO. Possible reasons for these observations are discussed later in this section.

Understanding change in λ_f of fluids at high P is important to predict the T rise under EHL conditions.[57] The change in calculated λ_f with $\dot{\gamma}$ for PAO and DCMP at 0.5 GPa and 1.0 GPa is shown in Fig. 4. Results are only shown for systems and conditions where a significant T_f rise occurs within the film in Fig. 3 ($v_s > 5$ m s^{-1}). Previous NEMD simulations of LJ fluids showed that λ_f is only weakly dependent on $\dot{\gamma}$.[68] Similarly, Fig. 4 shows no clear trend between λ_f and $\dot{\gamma}$ for the molecular fluids studied here. However, Fig. 4 shows that λ_f is dependant on both molecular structure and P. Specifically, λ_f of PAO increased with increasing P from 0.13 W m^{-1} K^{-1} at 0.5 GPa to 0.16 W m^{-1} K^{-1} at 1.0 GPa. The same trend was observed in Fig. 4 for DCMP; λ_f

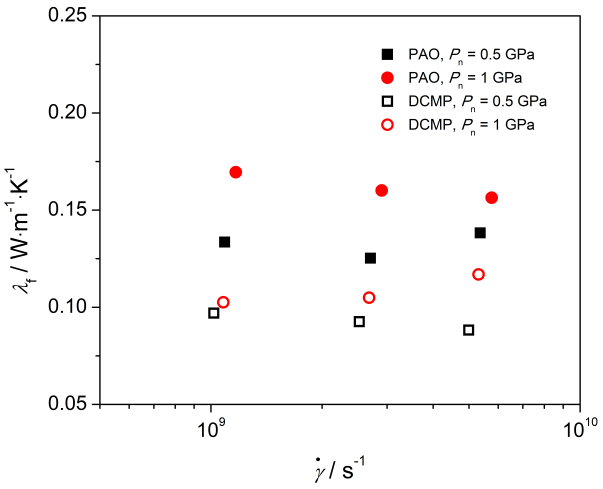

Fig. 4 Variation in λ_f with log($\dot{\gamma}$) for PAO and DCMP at 0.5 GPa and 1.0 GPa (symmetrical systems). The values of λ_f calculated from the T_f profiles in Fig. 3.

increases from 0.09 W m^{-1} K^{-1} at 0.5 GPa to 0.12 W m^{-1} K^{-1} at 1.0 GPa. Transient hot-wire experiments have been performed to investigate the effect of P on λ_f for both PAO[57] and DCMP[57,69] without shear applied. It is important to note that the experimental fluids differed to the pure molecules used in the simulations, which could affect λ_f. Specifically, DCMP contained polymer additives (Santotrac 50) while the PAO used had a higher viscosity grade ($\approx$ 20 cSt at 100 °C) and was a mixture of different molecular weights.[30] Despite these differences, qualitative agreement is expected between the experiments and simulations. The experiments showed that, in the ranges studied (T = 295-380 K, P = 0.1-1.1 GPa) λ_f was insensitive to T but varied strongly with molecular structure and P.[57] In the experiments for PAO, λ_f increased from 0.25 W m^{-1} K^{-1} at 0.5 GPa to 0.32 W m^{-1} K^{-1} at 1.0 GPa, while for DCMP it increased from 0.17 W m^{-1} K^{-1} to 0.24 W m^{-1} K^{-1}.[57] Thus, although λ_f is underestimated in Fig. 4 relative to experiments, λ_f increases with increasing P and is higher for PAO than DCMP in both the NEMD simulations and experiments. The lower λ_f from the NEMD simulations compared to the experiments could perhaps be due the differences in molecular composition described above. Another possible contribution to the difference is the reduced number of degrees of freedom in the UA force-field, which is has been shown in previous MD simulations to lead to underestimations of λ_f.[70]

Over the wide range of P and $\dot{\gamma}$ conditions studied here, there is a significant ($\approx$ 20 %) variation in ρ_f (see ESI). Through consideration of hard-sphere theory, λ_f has been correlated with ρ_f for n-alkanes.[71] Indeed, in these simulations, ρ_f is more sensitive to P compared to $\dot{\gamma}$ in the ranges studied (see ESI), which is the same as the trend observed for λ_f in Fig. 4. However, although PAO has a lower ρ_f than DCMP at equal P, it shows higher λ_f in Fig. 4, possibly due to its higher molecular flexibility.[21,32]

Fig. 5 shows the mean film T rise in the fluid, $\Delta\bar{T}_f$, *versus* log($\dot{\gamma}$) for PAO and DCMP at 0.5 and 1.0 GPa for the symmetrical sys-

tems. The inset shows same data on linear x-axis ($\dot{\gamma}$). The linear increase in $\Delta\bar{T}_f$ with $\dot{\gamma}$ in Fig. 5 is consistent with predictions using the Archard equation:[7]

$$\Delta\bar{T}_{total} = \Delta\bar{T}_s + \Delta\bar{T}_f = \left(\frac{1}{(2\pi\ \lambda_s\ \rho_s\ c_s)^{0.5}}\ t_i^{0.5}\ h + \frac{1}{(b\ \lambda_f)}\ h^2 \right)\ \bar{\tau}\ \dot{\gamma} \quad (3)$$

where $\Delta\bar{T}_s$ is the mean T rise in the surfaces. λ_s, ρ_s and c_s are the thermal conductivity, density and heat capacity of the solid surfaces respectively and t_i is the transit time of the surfaces across the contact.[5] The denominator on the right hand side of eqn (3), b, can vary broadly between 4 and 24.[10] A value of 8 implies that heat is generated evenly through the fluid film (i.e. Couette flow) while a value of 4 suggests that all of the heat is generated at the mid-plane.[5,7] Since $\Delta\bar{T}_s$ is negligible for the symmetrical systems (see Fig. 3), the gradients of the dotted lines in the Fig. 5 inset are equal to $(\bar{\tau}\ h^2)/(b\ \lambda_f)$. The gradient in Fig. 5 increases with increasing P and is significantly larger for DCMP compared to PAO. The larger $\Delta\bar{T}_f$ for DCMP compared to PAO is due to the lower λ_f (see Fig. 4),[57] as well as the higher $\bar{\tau}$; the latter point will be discussed in the Section 3.3.

Using the measured $\bar{\tau}$ (Section 3.3) and h as well as the λ_f calculated from the NEMD T_f profiles, the values of b for the linear fits in Fig. 5 could be determined. For PAO, b increased from 9.4 at 0.5 GPa to 10.3 at 1.0 GPa, while for DCMP, it increased from 11.0 at 0.5 GPa to 12.6 at 1.0 GPa. Note that the λ_f values calculated for the fluids and used in the fitting of b are somewhat lower than those measured experimentally.[57,69] All of the fluid-P combinations considered here exceed the value of 8 commonly used to predict $\Delta\bar{T}_f$ under EHL conditions. Interestingly, a b value of 9 was also used to fit recent experimental $\Delta\bar{T}_f$ *versus* $\dot{\gamma}$ results for DCMP under EHL conditions.[10] In these current simulations, b is larger for DCMP compared to PAO and increases with increasing P for both fluids. This suggests that the flow for DCMP deviates more from the commonly assumed Couette case and that higher P leads to larger deviations for both fluids; this will be further investigated in Section 3.2.

A linear increase in $\Delta\bar{T}_f$ with $\dot{\gamma}$ has also been observed in previous NEMD simulations of thin (h = 2.5 nm) n-hexadecane films at P = 0.5 GPa using a similar thermostatting strategy.[35] However, compared to this previous study,[35] the fluids used here show higher $\bar{\tau}$ and the films have a larger h. Consequently, a detectable $\Delta\bar{T}_f$ occurs at a lower $\dot{\gamma}$ and, at equal $\dot{\gamma}$, the magnitude of $\Delta\bar{T}_f$ is significantly larger than in ref.[35] These current results demonstrate that it is not possible to calculate a general 'critical $\dot{\gamma}$' at which shear heating will occur in NEMD simulations,[35] since this will also be dependent on h, $\bar{\tau}$, λ_f, as shown in eqn (3).[5,7] Thus it is recommended that $\Delta\bar{T}_f$ should be calculated on a case by case basis for confined NEMD simulations, particularly when relatively thick fluid films are employed.

3.1.2 Unsymmetrical Systems

For the unsymmetrical systems, in which the top slab has a longer thermostat coupling time, the T_f profile shape from the NEMD simulations can deviate from the symmetrical parabolas observed for the symmetrical systems. Despite this, the T_f profiles can still be fit quadratically using eqn (1). For example, Fig. 6 shows a representative example of the NEMD T_f profiles and quadratic fits for the unsymmetrical systems.

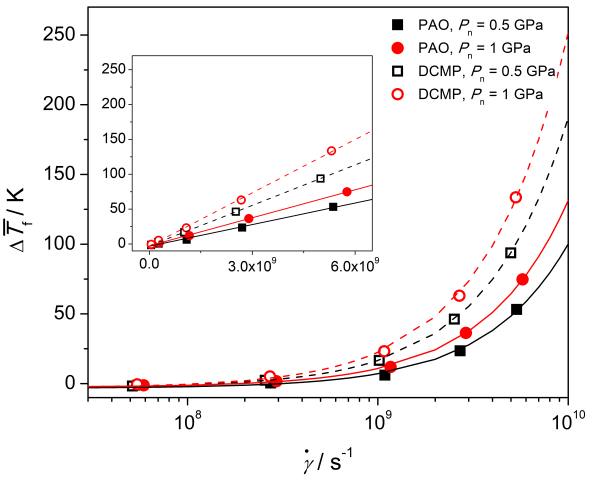

Fig. 5 $\Delta\bar{T}_f$ *versus* log($\dot{\gamma}$) for PAO and DCMP at 0.5 and 1.0 GPa (symmetrical systems). Inset shows same data on linear x-axis. Dotted lines represent Archard prediction from eqn (3). Both slabs thermostat coupling time of 0.1 ps. Statistical uncertainties are slightly smaller than symbol size.

Fig. 7 shows quadratic fits of the T_f profiles for PAO and DCMP at (a) 0.5 GPa and (b) 1.0 GPa for the different v_s considered. Here, the bottom slab thermostat coupling time is 0.1 ps and the top slab thermostat coupling time is 100 ps. Quadratic fits of the T_f profiles for intermediate thermostat coupling times on the top slab (1 and 10 ps) are shown in the ESI.

The circles in Fig. 7 show T_s for the top slab which has lower thermostat efficiency. In most cases, the top slab reaches a higher T than the thermostatted T, i.e. $T_s > 350$ K. Generally, $T_{s-f} \approx T_s$ since there is negligible thermal slip (i.e. insignificant Kapitza resistance) at the solid-liquid interface.[24] However, under the highest P and $\dot{\gamma}$ considered, some thermal slip occurs at the solid-liquid interface $T_{s-f} > T_s$, despite the fact that there is no velocity slip (see Fig. 10). Thermal slip has also been observed in the absence of velocity slip in previous NEMD simulations of strongly-confined atomic[72,73] and molecular[74,75] fluids. These current simulations demonstrate that such behavior is also possible in relatively thicker films at high P, but only under very extreme conditions.

In agreement with experiments[10] and numerical models[11–13] using two surfaces with different thermal properties, T_f is significantly higher close to the slab with lower thermal conductivity. The maximum T_f in Fig. 7, which is localized closer to the slab with lower thermostat efficiency, is larger than when both slabs have high thermostat efficiency (Fig. 3).

Using eqn (1), the quadratic fits of the T profiles in Fig. 7 resulted in similar values of λ_f as calculated from the symmetrical profiles. The λ_f values for the unsymmetrical systems used in the calculation of b from Fig. 8 are; 0.16 W m^{-1} K^{-1} and 0.18 W m^{-1} K^{-1} for PAO at 0.5 GPa and 1.0 GPa, and 0.10 W m^{-1} K^{-1} and

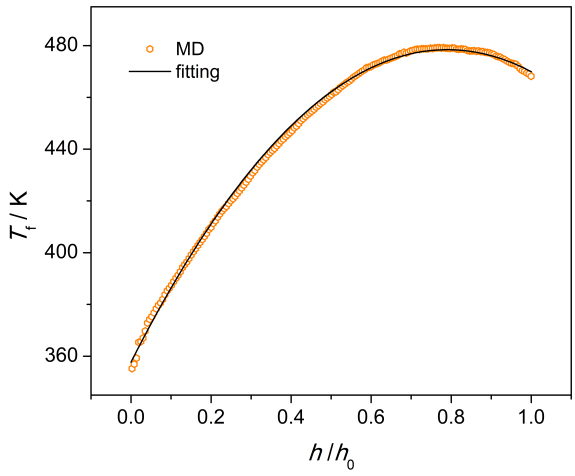

Fig. 6 Spatially resolved $T(z)$ profile for PAO at 0.5 GPa and 100 m s^{-1}. Bottom slab thermostat coupling time of 0.1 ps, top slab 100 ps (unsymmetrical system). Note that h is normalized. Solid line is quadratic fit using eqn (1).

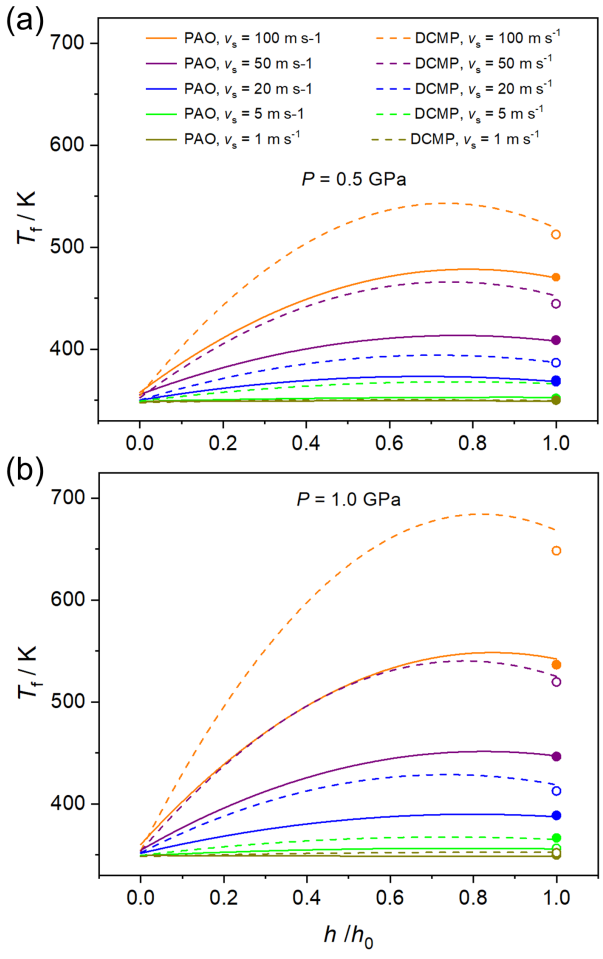

Fig. 7 Quadratic fits of the spatially resolved $T(z)$ profiles for PAO and DCMP at 0.5 GPa and 1.0 GPa for the different values of v_s considered. Bottom slab thermostat coupling time of 0.1 ps, top slab 100 ps (unsymmetrical systems). Note that h is normalized. Circles show T_s within the top slab.

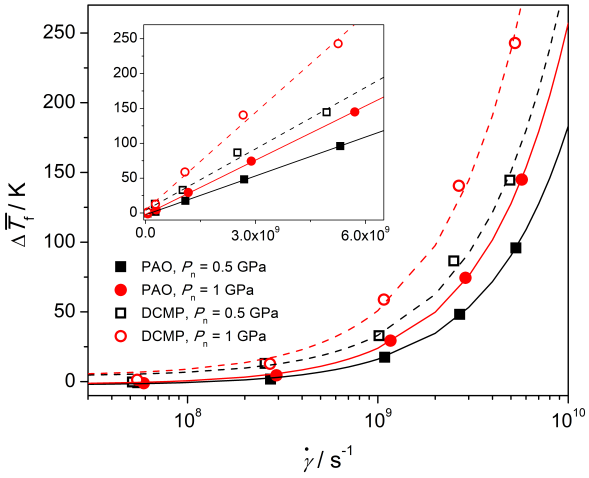

Fig. 8 Change in $\Delta\bar{T}_f$ with log($\dot{\gamma}$) for PAO and DCMP at 0.5 GPa and 1.0 GPa (unsymmetrical systems). Inset shows same data on linear x-axis. Dotted lines represent Archard prediction from eqn (3). Bottom slab thermostat coupling time of 0.1 ps, top slab 100 ps. Statistical uncertainties are slightly smaller than symbol size.

0.14 W m^{-1} K^{-1} for DCMP at 0.5 GPa and 1.0 GPa respectively.

Fig. 8 shows the change in $\Delta\bar{T}_f$ with log($\dot{\gamma}$) for PAO and DCMP at (a) 0.5 and (b) 1.0 GPa for the unsymmetrical systems. Comparing the symmetrical (Fig. 5) and unsymmetrical (Fig. 8) systems, a noticeable $\Delta\bar{T}_f$ occurs at lower $\dot{\gamma}$ for the latter, and the gradient of the increase in $\Delta\bar{T}_f$ with $\dot{\gamma}$ is steeper. For DCMP, the linear fits in Fig. 8 from eqn (3) require values of b which decrease from 5.0 at 0.5 GPa to 4.1 at 1.0 GPa for PAO, and from 4.1 at 0.5 GPa to 3.7 at 1.0 GPa for DCMP. These values are close to the value predicted by Archard (4) when all of the shear heating occurs in the mid-plane of the film.[5,7] In the unsymmetrical systems, the value of b is lower for DCMP compared to PAO and decreases with increasing pressure. This suggests that the flow for DCMP deviates more from the commonly assumed Couette case (8) compared to PAO and that higher P leads to larger deviations for both fluids; this will be further investigated in Section 3.2.

3.2 Flow

The flow, v_x, profiles are block averaged and spatially binned in the z-direction. In all of the flow profiles, h and v_s are normalized between the different systems to aid comparison.

3.2.1 Symmetrical Systems

Fig. 9 shows the spatially resolved flow, $v_x(z)$, profiles for PAO and DCMP at (a) 0.5 GPa and (b) 1.0 GPa for some of the v_s values considered for the symmetrical systems. Flow profiles from the other v_s values are shown in the ESI for completeness. In all cases, the outer molecular layers of fluid moves at the same velocity as the sliding slabs, indicating that no boundary slip occurs.[32] At low P and low v_s, PAO and DCMP both show linear Couette flow, with the first few molecular layers (see ESI) moving at the same velocity as the α-Fe surfaces. At low P and high v_s, both fluids show cubic flow profiles, indicating that the outer

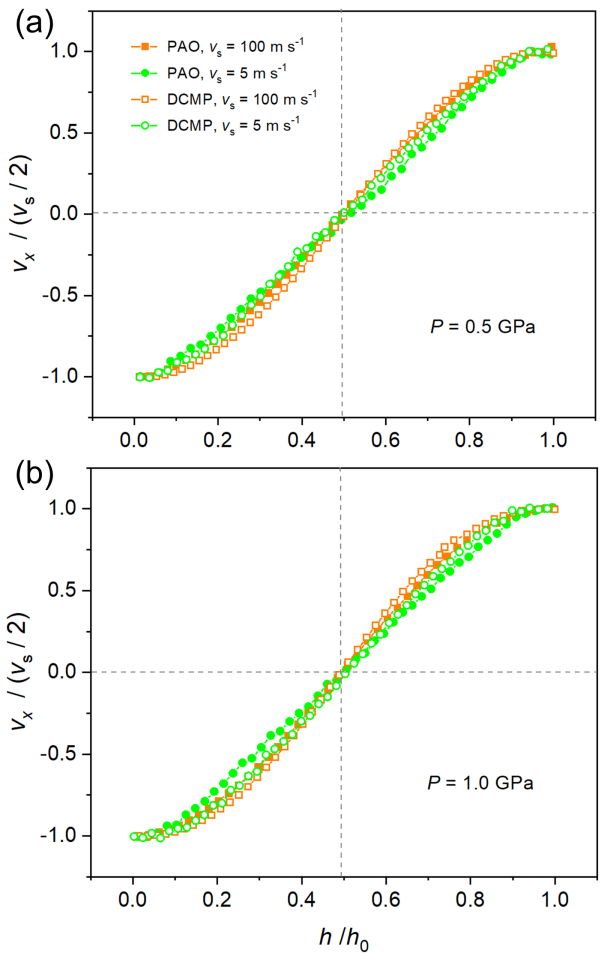

Fig. 9 Spatially resolved flow, $v_x(z)$, profiles for PAO and DCMP at (a) 0.5 GPa and (b) 1.0 GPa and 5 m s^{-1} and 100 m s^{-1} (other v_s in ESI). Both slabs thermostat coupling time of 0.1 ps (symmetrical systems). Note that h and v_s are normalized.

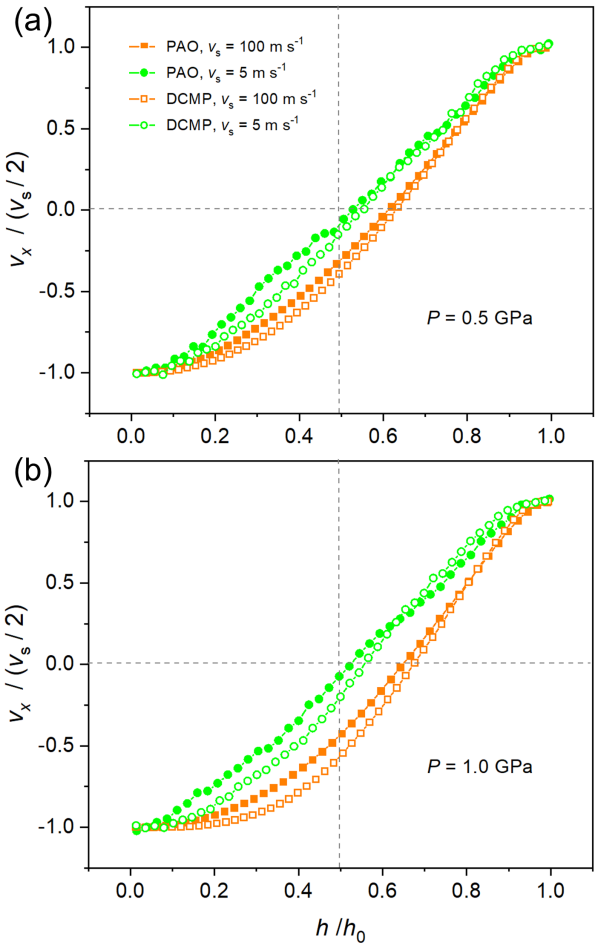

Fig. 10 Spatially resolved flow, $v_x(z)$, profiles for PAO and DCMP at (a) 0.5 GPa and (b) 1.0 GPa and 5 m s^{-1} and 100 m s^{-1} (other v_s in ESI). Bottom slab thermostat coupling time of 0.1 ps, top slab 100 ps (unsymmetrical systems). Note that h and v_s are normalized.

regions of the fluid are sheared less than the center of the film; this behavior is known as 'central localization' (CL).[24] In these simulations, h = 17-20 nm, so Fig. 9 shows that the 'unsheared' region extends further into the fluid than the direct influence of the surfaces (Fe σ = 0.2321 nm).[32] At high P, PAO still shows a Couette-like profile at low v_s, but shows strong CL at high v_s. At high P, DCMP shows strong CL at both low and high v_s. CL has also been observed in previous NEMD simulations of atomic LJ fluids[24–26], glasses,[27] molecular fluids,[32,33] and polymers,[28] as well as experiments using polymers.[15–17,19]

In Fig. 11, DCMP shows stronger CL compared to PAO, in agreement with previous NEMD simulations which compared lubricants and traction fluids.[32] In common with previous experiments[19] and NEMD simulations,[32,33] the deviations from planar Couette flow are more significant at high P (Fig. 9b) compared to at low P (Fig. 9a). Previous experiments have highlighted two distinct forms of CL which could occur in fluids under EHL conditions; one mechanically induced[15] and the other thermally induced (adiabatic).[16] Unlike the mostly isothermal NEMD simulations in ref.[32], shear localization in these simulations is stronger at higher v_s, where the T_f in the center of the fluid is much higher than in the fluid near the slabs (Fig. 3). In these simulations, PAO shows only adiabatic CL[16] at high v_s when a significant $\Delta\bar{T}_f$ occurs within the film (Fig. 3). Adiabatic CL[16] is also observed for DCMP at high P and high v_s; however, it also shows mechanical CL[15] at high P and low v_s where negligible $\Delta\bar{T}_f$ occurs within the film (Fig. 3). At 1.0 GPa and 350 K, DCMP is expected to be in a glassy state,[57] suggesting that vitrification could be the precursor to mechanical shear localization.[17]

3.2.2 Unsymmetrical Systems

Fig. 10 shows the spatially resolved flow profiles for PAO and DCMP at (a) 0.5 GPa and (b) 1.0 GPa for some of the v_s values considered for the unsymmetrical systems. Flow profiles from other v_s values are shown in the ESI for completeness.

Fig. 10 shows that even when the thermostat efficiency in the top slab is reduced, the flow profiles remain mostly Couette-like for both fluids at low P and v_s. However, at high P and v_s, both fluids are sheared more close to the slab with lower thermostat efficiency. The flow asymmetry can be directly attributed to the T_f asymmetry shown in Fig. 7. Previous NEMD simulations for LJ fluids have also shown asymmetric flow profiles, which was

referred to as asymmetric melting (AM).[25,26] In these previous simulations, AM was caused by surfaces different wettability[25] and roughness,[26] rather than thermostat efficiency.

In Fig. 10, the flow asymmetry is more significant under for systems and conditions where $\Delta\bar{T}_f$ is larger in Fig. 8. More specifically, the flow profiles show more asymmetry: i) for DCMP compared to PAO, ii) at higher P, and iii) at higher v_s.

3.3 Friction

To mimic tribology experiments, $\bar{\tau}$ in the NEMD simulations was monitored through the mean lateral (friction) force acting on the outer layer of atoms in the top and bottom slabs in response to the fluid.[32] For every state point, three independent trajectories were generated using different initial velocities, the points and error bars represent the mean and one standard deviation of these results.

3.3.1 Symmetrical Systems

Fig. 11 shows that $\bar{\tau}$ is significantly higher for the traction fluid, DCMP, compared to the lubricant, PAO, for all of the symmetrical systems. However, the difference in $\bar{\tau}$ between the two fluids decreases as $\dot{\gamma}$ increases. The values of $\bar{\tau}$ are in general agreement with previous NEMD simulations which employed a far more computationally expensive AA force-field.[32] For both fluids, $\bar{\tau}$ increases with increasing P, in agreement with Amontons' friction law.[76] For PAO at low P, $\bar{\tau}$ increases linearly with $\log(\dot{\gamma})$, as is commonly observed in tribology experiments of lubricants under EHL conditions.[5,6,21,32] Such behavior is also consistent with recent bulk NEMD simulations of the branched alkane squalane under EHL conditions.[31]

For DCMP at 1.0 GPa, $\bar{\tau}$ is insensitive to $\dot{\gamma}$ in the range studied, suggesting that the limiting shear stress (LSS) has been reached.[53] The LSS has commonly been observed experimentally and in NEMD simulations of bulky, inflexible traction fluid molecules.[21,32,34] Importantly, in Fig. 11 the insensitivity of $\bar{\tau}$ to $\dot{\gamma}$ occurs even when $\dot{\gamma} < 10^9$ s^{-1}, where there is negligible shear heating ($\Delta\bar{T}_f < 10$ K), as shown in Fig. 5. Since 1.0 GPa is above the glass transition P for DCMP at 350 K,[57] this suggests that vitrification could be the physical driving force for both mechanical CL (Section 3.2) and ultimately also the LSS behavior.[34]

The other two P-fluid combinations (PAO at 1.0 GPa and DCMP at 0.5 GPa) appear to be intermediate cases; $\bar{\tau}$ first increases linearly with $\log(\dot{\gamma})$ and then asymptotes when $\dot{\gamma} > 10^9$ s^{-1}. Looking at Fig. 5, this coincides with the $\dot{\gamma}$ at which significant shear heating ($\Delta\bar{T}_f > 10$ K) occurs within the film. The insensitivity of $\bar{\tau}$ to $\dot{\gamma}$ in these cases is thus likely to be a direct result of shear heating.

In ref.[34], $\Delta\bar{T}_f$ was assumed to be negligible below 10^{10} s^{-1} on the basis of confined NEMD simulations of thin (2.5 nm) n-hexadecane films using a similar thermostatting strategy to that employed here. However, the current NEMD simulations suggest that in ref.[34] where $h = 8$-14 nm, significant shear heating ($\Delta\bar{T}_f >$ 10 K) was likely when $\dot{\gamma} \geq 10^9$ s^{-1}. Moreover, the experimental results purporting to show the LSS for lubricant at 313 K and 1.2 GPa, which agree with the aforementioned NEMD simulations,[34] are unlikely to be isothermal under such conditions and do not appear to have been thermally corrected.[5,6,21,32] Previous tribology

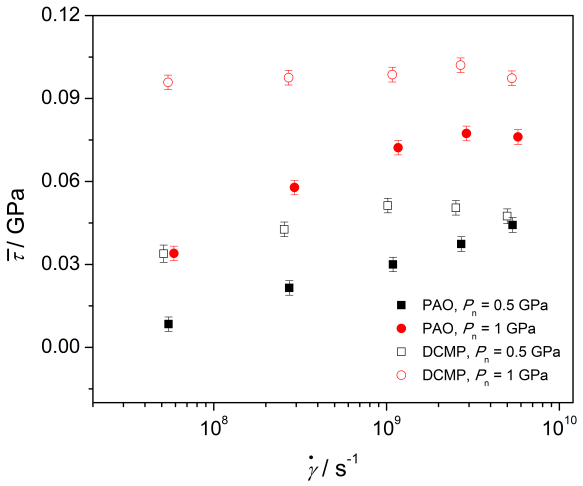

Fig. 11 Change in $\bar{\tau}$ with $\log(\dot{\gamma})$ for PAO and DCMP at 0.5 and 1.0 GPa (symmetrical systems). Both slabs thermostat coupling time of 0.1 ps. Error bars show one standard deviation between three independent NEMD trajectories.

experiments have shown that, compared to traction fluids, the $\bar{\tau}$ of lubricants such as squalane under EHL conditions is rather sensitive to $\Delta\bar{T}_f$.[5,21,32] Consequently, in both the simulations and experiments for squalane in ref.,[34] it is difficult to definitively state that the independence of $\bar{\tau}$ to $\dot{\gamma}$ is due to the LSS being reached, as opposed to shear heating.

In contrast to DCMP, the slope of the increase of $\bar{\tau}$ with $\log(\dot{\gamma})$ for PAO is similar at both 0.5 GPa and 1.0 GPa in Fig. 11. This suggests that PAO at 350 K is still far from reaching a LSS at 1.0 GPa.[53] Experiments have shown that glass transition P of PAO will be $>$ 1.0 GPa at 350 K,[57] further supporting a link between the two phenomena.[34]

3.3.2 Unsymmetrical Systems

Fig. 12 shows the change in $\bar{\tau}$ with $\log(\dot{\gamma})$ for PAO and DCMP at 0.5 GPa and 1.0 GPa for the unsymmetrical systems. Generally, $\bar{\tau}$ first increases and then decreases with $\log(\dot{\gamma})$. The friction curves are qualitatively similar to those observed in previous tribology experiments and numerical models where significant $\Delta\bar{T}_f$ occurs due to the use of surfaces with low thermal conductivity.[11,12] When $\dot{\gamma} < 10^9$ s^{-1} and $\Delta\bar{T}_f$ is negligible, $\bar{\tau}$ does not change compared to the symmetrical systems in Fig. 11 within statistical uncertainty. However, when $\dot{\gamma} > 10^9$ s^{-1}, $\bar{\tau}$ is significantly lower in Fig. 12 compared to Fig. 11 Comparing, Fig. 5 and Fig. 8, the lower $\bar{\tau}$ can be partially attributed to the larger $\Delta\bar{T}_f$ due to the lower thermostat efficiency in the top slab. Additionally, the steeper velocity gradient in Fig. 10 compared to Fig. 9 will lead to enhanced shear thinning, further reducing $\bar{\tau}$.[32] The $\bar{\tau}$ results in Fig. 12 support numerical models which suggested that the application of insulating surface coatings can significantly reduce EHL friction when the $\Delta\bar{T}_f$ becomes significant.[11–13] These NEMD simulations also suggest that at high P and $\dot{\gamma}$, the lubricant λ_f as well as its rheology, contributes to the observed frictional response.

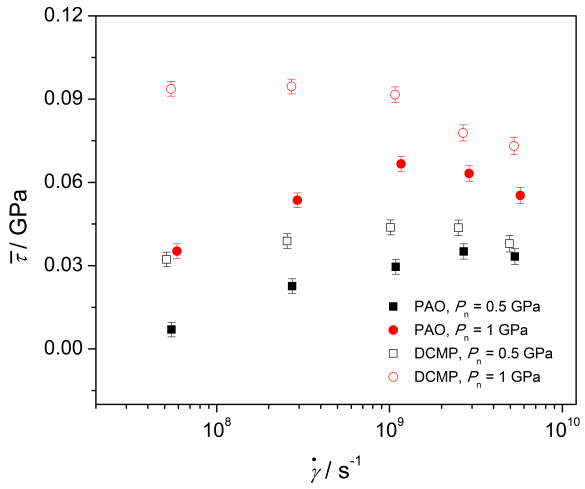

Fig. 12 Change in $\bar{\tau}$ with log($\dot{\gamma}$) for PAO and DCMP at 0.5 and 1.0 GPa (unsymmetrical systems). Bottom slab thermostat coupling time of 0.1 ps, top slab 0.1-100 ps.

4 Conclusions

In this study, NEMD simulations have been used to investigate the effect of surface and lubricant properties on the spatially resolved flow and T_f profiles, as well as friction, under high P and $\dot{\gamma}$, EHL conditions. In common with tribology experiments, flexible lubricant molecules (PAO) give low $\bar{\tau}$, which increases linearly with log($\dot{\gamma}$). Conversely, bulky traction fluids (DCMP) show higher $\bar{\tau}$, but a shallower slope of increase of $\bar{\tau}$ with log($\dot{\gamma}$). Indeed, at high P (1.0 GPa), which is expected to exceed the glass transition P for DCMP at 350 K, $\bar{\tau}$ becomes insensitive to log($\dot{\gamma}$), indicating that the LSS has been reached. Compared to PAO, DCMP shows more significant shear heating and stronger shear localization. Adiabatic shear localization is observed for both fluids at high $\dot{\gamma}$, while DCMP also shows mechanical shear localization at high P and low $\dot{\gamma}$.

The spatially resolved T_f profiles from the NEMD simulations can be fit quadratically using the Fourier law of heat conduction. The curvature of these profiles can be used to calculate λ_f, which increases with P and is significantly higher for PAO compared to DCMP, in agreement with experimental measurements. The $\Delta\bar{T}_f$ increases linearly with $\dot{\gamma}$, as predicted by the Archard equation for EHL T rise. Moreover, this study demonstrates the potential for NEMD simulations to be used to verify the parameters used in the Archard equation to predict $\Delta\bar{T}_f$ in tribology experiments.

When the thermal dissipation efficiency of one of the surfaces is reduced, by increasing the thermostat coupling time, the flow and T profiles become strongly asymmetric. The larger T rises and steeper v_x gradient in this case leads to large reductions in friction, particularly at high P and $\dot{\gamma}$. The simulations support the postulation that insulating surfaces such as DLC and ceramics can significantly reduce friction under such conditions without inducing velocity slip. Under such conditions, the lubricant λ_f as well as its rheology, contributes to the observed friction response. This study demonstrates the ability of NEMD simulations to simultaneously probe the shear heating, flow and friction behaviour of fluids under extreme conditions. The molecular-scale insights provided by this study improve understanding of fluid behaviour under EHL conditions in symmetric and unsymmetrical contacts.

Conflicts of Interest

There are no conflicts to declare.

Acknowledgements

The authors thank B. D. Todd, D. M. Heyes, and Hugh A. Spikes for useful discussions. H.G. thanks the Alexander von Humboldt Foundation for a Humboldt Research Fellowship. J.P.E. thanks the Engineering and Physical Sciences Research Council (EPSRC) for a Doctoral Prize Fellowship. D.D. thanks the EPSRC for an Established Career Fellowship EP/N025954/1 and grant EP/P030211/1. Simulations were facilitated via the Imperial College London Research Computing Service (RCS). All data reported in the manuscript can be obtained by emailing the corresponding author or tribology@imperial.ac.uk.

References

1 L. Bocquet and E. Charlaix, *Chem. Soc. Rev.*, 2009, **39**, 1073–1095.
2 R. I. Taylor, *Faraday Discuss.*, 2012, **156**, 361–382.
3 S. Granick, *Science.*, 1991, **253**, 1374–1379.
4 K. Holmberg and A. Erdemir, *Friction*, 2017, **5**, 263–284.
5 H. Spikes and Z. Jie, *Tribol. Lett.*, 2014, **56**, 1–25.
6 C. R. Evans and K. L. Johnson, *Proc. Inst. Mech. Eng. C*, 1986, **200**, 303–312.
7 J. Archard, *Wear*, 1959, **2**, 438–455.
8 P. M. Cann and H. A. Spikes, *Tribol. Trans.*, 1989, **3**, 414–422.
9 T. Reddyhoff, H. A. Spikes and A. V. Olver, *Proc. Inst. Mech. Eng. Part J: J. Eng. Tribol.*, 2009, **223**, 1165–1177.
10 J. Lu, T. Reddyhoff and D. Dini, *Tribol. Lett.*, 2018, **66**, 7.
11 M. Björling, P. Isaksson, P. Marklund and R. Larsson, *Tribol Lett*, 2012, **47**, 285–294.
12 M. Björling, W. Habchi, S. Bair, R. Larsson and P. Marklund, *Tribol. Lett.*, 2014, **53**, 477–486.
13 M. Kaneta, P. Sperka, P. Yang, I. Krupka, P. Yang and M. Hartl, *Tribol. Trans.*, 2018, **61**, 869–879.
14 M. A. Plint, *Proc. Inst. Mech. Eng.*, 1967, **182**, 300–306.
15 S. Bair, F. Qureshi and W. O. Winer, *J. Tribol.*, 1993, **115**, 507–514.
16 S. Bair, F. Qureshi and M. Khonsari, *J. Tribol.*, 1994, **116**, 705.
17 S. Bair and C. McCabe, *Tribol. Int.*, 2004, **37**, 783–789.
18 A. Ponjavic, L. di Mare and J. S. S. Wong, *J. Polym. Sci. B Polym. Phys.*, 2014, **52**, 708–715.
19 B. Galmiche, A. Ponjavic and J. S. S. Wong, *J. Phys. Condens. Matter*, 2016, **28**, 134005.
20 S. Jeffreys, L. di Mare, N. Morgan and J. S. S. Wong, *RSC Advances*, 2019, **9**, 1441–1450.
21 J. Zhang, A. Tan and H. Spikes, *Tribol. Lett.*, 2017, **65**, 13.
22 W. T. Ashurst and W. G. Hoover, *Phys. Rev. A*, 1975, **11**, 658–678.

23 J. P. Ewen, D. M. Heyes and D. Dini, *Friction*, 2018, **6**, 349–386.

24 D. M. Heyes, E. R. Smith, D. Dini, H. A. Spikes and T. A. Zaki, *J. Chem. Phys.*, 2012, **136**, 134705.

25 C. Gattinoni, D. M. Heyes, C. D. Lorenz and D. Dini, *Phys. Rev. E*, 2013, **88**, 052406.

26 S. Maćkowiak, D. M. Heyes, D. Dini and A. C. Brańka, *J. Chem. Phys.*, 2016, **145**, 164704.

27 F. Varnik, L. Bocquet, J.-L. Barrat and L. Berthier, *Phys. Rev. Lett.*, 2003, **90**, 095702.

28 J. Cao and A. E. Likhtman, *Phys. Rev. Lett.*, 2012, **108**, 028302.

29 S. Bair, C. McCabe and P. T. Cummings, *Phys. Rev. Lett.*, 2002, **88**, 058302.

30 P. Liu, J. Lu, H. Yu, N. Ren, F. E. Lockwood and Q. J. Wang, *J. Chem. Phys.*, 2017, **147**, 084904.

31 V. Jadhao and M. O. Robbins, *Proc. Natl. Acad. Sci.*, 2017, **114**, 7952–7957.

32 J. P. Ewen, C. Gattinoni, J. Zhang, D. M. Heyes, H. A. Spikes and D. Dini, *Phys. Chem. Chem. Phys.*, 2017, **19**, 17883–17894.

33 H. Washizu, T. Ohmori and A. Suzuki, *Chem. Phys. Lett.*, 2017, **678**, 1–4.

34 A. Porras-Vazquez, L. Martinie, P. Vergne and N. Fillot, *Phys. Chem. Chem. Phys.*, 2018, **20**, 27280–27293.

35 H. Berro, N. Fillot, P. Vergne, T. Tokumasu, T. Ohara and G. Kikugawa, *J. Chem. Phys.*, 2011, **135**, 134708.

36 S. Plimpton, *J. Comput. Phys.*, 1995, **117**, 1 – 19.

37 M. G. Martin and J. I. Siepmann, *J. Phys. Chem. B*, 1998, **102**, 2569–2577.

38 W. Humphrey, A. Dalke and K. Schulten, *J. Mol. Graph. Model.*, 1996, **14**, 33–38.

39 W. D. Cornell, P. Cieplak, C. I. Bayly, I. R. Gould, K. M. Merz, D. M. Ferguson, D. C. Spellmeyer, T. Fox, J. W. Caldwell and P. A. Kollman, *J. Am. Chem. Soc.*, 1995, **117**, 5179–5197.

40 B. L. Eggimann, A. J. Sunnarborg, H. D. Stern, A. P. Bliss and J. I. Siepmann, *Mol. Simul.*, 2014, **40**, 101–105.

41 J. E. Lennard-Jones, *Proc. R. Soc. A*, 1924, **106**, 463–477.

42 H. A. Lorentz, *Ann. Phys.*, 1881, **248**, 127–136.

43 D. Berthelot, *Comptes. Rendus. Acad. Sci.*, 1898, **126**, 1703–1855.

44 M. G. Martin and J. I. Siepmann, *J. Phys. Chem. B*, 1999, **103**, 4508–4517.

45 S. J. Keasler, S. M. Charan, C. D. Wick, I. G. Economou and J. I. Siepmann, *J. Phys. Chem. B*, 2012, **116**, 11234–11246.

46 J. P. Ewen, C. Gattinoni, F. M. Thakkar, N. Morgan, H. A. Spikes and D. Dini, *Materials*, 2016, **9**, 651.

47 W. Allen and R. L. Rowley, *J. Chem. Phys.*, 1997, **106**, 10273–10281.

48 C. McCabe, S. T. Cui, P. T. Cummings, P. A. Gordon and R. B. Saeger, *J. Chem. Phys.*, 2001, **114**, 1887–1891.

49 M. I. Mendelev, S. Han, D. J. Srolovitz, G. J. Ackland, D. Y. Sun and M. Asta, *Philos. Mag.*, 2003, **83**, 3977–3994.

50 D. Savio, N. Fillot, P. Vergne and M. Zaccheddu, *Tribol. Lett.*, 2012, **46**, 11–22.

51 A. Ponjavic, J. Dench, N. Morgan and J. S. S. Wong, *RSC Adv.*, 2015, **5**, 99585.

52 J. Dench, L. di Mare, N. Morgan and J. S. S. Wong, *Phys. Chem. Chem. Phys.*, 2018, **20**, 30267–30280.

53 L. Martinie and P. Vergne, *Tribol. Lett.*, 2016, **63**, 21.

54 M. L. Gee, P. M. McGuiggan, J. N. Israelachvili and A. M. Homola, *J. Chem. Phys.*, 1990, **93**, 1895–1906.

55 M. Kasuya, K. Tomita, M. Hino, M. Mizukami, H. Mori, S. Kajita, T. Ohmori, A. Suzuki and K. Kurihara, *Langmuir*, 2017, **33**, 3941–3948.

56 C. Gattinoni, S. Maćkowiak, D. M. Heyes, A. C. Branka and D. Dini, *Phys. Rev. E*, 2014, **90**, 043302.

57 R. Larsson and O. Andersson, *Proc. Inst. Mech. Eng. Part J: J. Eng. Tribol.*, 2000, **214**, 337–342.

58 R. Taylor and B. de Kraker, *Proc. Inst. Mech. Eng. Part J: J. Eng. Tribol.*, 2017, **231**, 1106–1116.

59 T. Schneider and E. Stoll, *Phys. Rev. B*, 1978, **17**, 1302–1322.

60 R. Khare, J. de Pablo and A. Yethiraj, *J. Chem. Phys.*, 1997, **107**, 2589.

61 B. D. Todd, D. J. Evans, K. P. Travis and P. J. Daivis, *J. Chem. Phys.*, 1999, **111**, 10730–10731.

62 S. Bernardi, B. D. Todd and D. J. Searles, *J. Chem. Phys.*, 2010, **132**, 244706.

63 X. Yong and L. T. Zhang, *J. Chem. Phys.*, 2013, **138**, 084503.

64 S. J. Eder, U. Cihak-Bayr, D. Bianchi, G. Feldbauer and G. Betz, *ACS Appl. Mater. Interfaces*, 2017, **9**, 13713–13725.

65 T. Reddyhoff, A. Schmidt and H. Spikes, *Tribol. Lett.*, 2019, **67**, 22.

66 B. Y. Cao, *J. Chem. Phys.*, 2008, **129**, 074106.

67 F. Bresme and J. Armstrong, *J. Chem. Phys.*, 2014, **140**, 016102.

68 P. J. Daivis and D. J. Evans, *Phys. Rev. E*, 1993, **48**, 1058–1065.

69 J. Richmond, O. Nilsson and O. Sandberg, *J. Appl. Phys.*, 1984, **56**, 2065.

70 M. Zhang, E. Lussetti, E. S. de Souza and F. Müller-Plathe, *J. Phys. Chem. B*, 2005, **109**, 15060–15067.

71 M. J. Assael, J. H. Dymond, M. Papadaki and P. M. Patterson, *Int. J. Thermophys.*, 1992, **13**, 269–281.

72 T. Ohara and D. Torii, *J. Chem. Phys.*, 2005, **122**, 214717.

73 B. H. Kim, A. Beskok and T. Cagin, *Microfluid. Nanofluidics*, 2010, **9**, 31–40.

74 R. Khare, P. Keblinski and A. Yethiraj, *Int. J. Heat Mass Transf.*, 2006, **49**, 3401–3407.

75 A. R. bin Saleman, H. K. Chilukoti, G. Kikugawa, M. Shibahara and T. Ohara, *Int. J. Therm. Sci.*, 2017, **120**, 273–288.

76 J. Gao, W. D. Luedtke, D. Gourdon, M. Ruths, J. N. Israelachvili and U. Landman, *J. Phys. Chem. B.*, 2004, **108**, 3410–3425.